East European Journal of Physics. 4. 484-495 (2025)
DOI:10.26565/2312-4334-2025-4-49 ISSN 2312-4334

PHASE TRANSFORMATIONS AND STRUCTURAL TRANSFORMATIONS OF MANGANESE SILICIDES IN THE Si-MN SYSTEM

Sh.B. Utamuradova, Sh.Kh. Daliev, J.J. Khamdamov, Kh.J. Matchonov*, A.Kh. Khaitbaev
Institute of Semiconductor Physics and Microelectronics, National University of Uzbekistan,
20 Yangi Almazar st., Tashkent, Uzbekistan
**Corresponding Author e-mail: husniddin94_04@bk.ru*
Received August 31, 2025; revised October 8, 2025; accepted October 12, 2025

A comprehensive investigation of thermally induced phase transformations in the silicon-manganese (Si–Mn) system was conducted. The study utilized X-ray diffraction (XRD), Raman spectroscopy (including chemical Raman mapping), scanning electron microscopy with energy-dispersive X-ray spectroscopy (SEM–EDS), deep-level transient spectroscopy (DLTS), and thermodynamic CALPHAD modeling. The sequence of transformations has been reliably reconstructed as follows: (i) interstitial incorporation of Mn and partial amorphization of the near-surface Si layer; (ii) nucleation and growth of MnSi (B20 structure, $P2_13$); (iii) stabilization of the higher silicide phase Mn_4Si_7 under Si-rich conditions; (iv) at T ≫ 900 °C, a partial reverse transformation to MnSi. DLTS analysis revealed three electrically active deep-level centers with activation energies of Ec–0.53 eV, Ec–0.43 eV, and Ec–0.20 eV ($\sigma_n \approx 10^{-16}$–$10^{-15}$ cm²), which correlate with the MnSi → Mn_4Si_7 transition and interface traps at the "silicide/Si" boundary. CALPHAD modeling confirmed negative Gibbs free energies of formation (ΔGf) and identified thermodynamic stability windows for MnSi (600–750 °C) and Mn_4Si_7 (800–950 °C). The resulting process map provides the technological parameters for synthesizing CMOS-compatible Si–Mn structures.
Keywords: *Silicon; Manganese; Manganese Silicides; MnSi; Mn_4Si_7; Phase transformations; XRD; Raman; SEM–EDS; DLTS; CALPHAD; Gibbs free energy*
PACS: 68.37.Hk, 33.20.Fb

INTRODUCTION

Doping silicon with transition metals is a strategically important direction in the engineering of functional semiconductor materials, aimed at broadening the spectrum of its electronic, magnetic, and thermal properties. Among the wide range of 3D-elements, manganese attracts particular attention due to its ability to form stable silicide phases, as well as to induce spin-dependent conductivity and weak ferromagnetism in the Si matrix [1-5]. The silicon-manganese (Si–Mn) system is a complex binary system characterized by a rich phase diagram with numerous intermetallic compounds of variable composition. The most studied and practically significant phases are MnSi (cubic B20 structure), Mn_4Si_7 (tetragonal), and more silicon-rich compounds such as $Mn_{11}Si_{19}$ [6-9].

These silicides are distinguished by their high thermal and chemical stability, low specific thermal conductivity, and pronounced anisotropic magnetotransport properties, including the spin-filtering effect and the anomalous Hall effect [10-14]. This combination of properties makes them candidates for applications in the fields of spintronics, thermoelectric converters, and CMOS-compatible nanoelectronic platforms [15-18].

Despite the existence of a significant body of experimental and theoretical data on the Si–Mn system, several key issues remain unresolved. The mechanisms and temperature thresholds of phase transitions during thermal processing have not been fully established. The localization of manganese atoms in the early stages of annealing (including interstitial and cluster states) is unclear. The formation conditions of the Mn_4Si_7 phase and its possible transformation back to MnSi upon further heating are insufficiently studied, as is the influence of non-stoichiometry and internal stresses on the stability of silicide phases.

A particular challenge is the reliable identification of the early stages of silicide formation at low temperatures, where Mn may still exist in a disordered form or as a dissolved atom in a-Si. Such states are difficult to distinguish using XRD methods but can be partially detected using highly sensitive vibrational spectroscopies (in particular, Raman) [18-21]. Furthermore, the use of a thermodynamic approach to analyzing phase equilibria, based on the CALPHAD (CALculation of PHAse Diagrams) methodology, is of critical importance. This approach allows for the prediction of silicide stability based on the Gibbs free energy of formation and the modeling of binary phase diagrams [21-25]. A comprehensive investigation of thermally induced phase transformations in the Si–Mn system, involving both experimental methods (XRD, Raman, XPS) and computational modeling (CALPHAD), is necessary to construct a complete picture of the phase evolution. This not only contributes to a deeper understanding of the fundamental processes of doping and diffusion in semiconductors but also opens up possibilities for the predictable synthesis of functional nanostructures with desired properties.

Thus, the investigation of phase formation and phase stability of manganese silicides in doped silicon films as a function of annealing conditions is a relevant task at the intersection of solid-state physics, materials science, and applied nanotechnology.

Cite as: Sh.B. Utamuradova, Sh.Kh. Daliev, J.J. Khamdamov, Kh.J. Matchonov, A.Kh. Khaitbaev, East Eur. J. Phys. 4, 484 (2025), https://doi.org/10.26565/2312-4334-2025-4-49

MATERIALS AND METHODS

The starting materials were single-crystalline p-type and n-type silicon wafers with resistivities ranging from 5 to 35 Ω·cm. Doping with high-purity (≥ 99.999%) metallic manganese was performed by thermal vacuum evaporation in a high vacuum environment ($P \leq 10^{-7}$–10^{-8} Torr), maintained by an oil-free turbomolecular pumping system. Manganese doping was carried out through high-temperature annealing in sealed vacuum quartz ampules at temperatures ranging from 600 to 1200 °C for durations of 0.5 to 10 hours. Upon completion of the heat treatment, the samples were subjected to either rapid quenching or slow furnace cooling. These different thermal trajectories allowed for the simulation of both near-equilibrium and metastable conditions for crystallization and phase transformation, which significantly influence the morphology of the silicide phases and the distribution of Mn within the Si matrix [25, 26].

Vibrational properties were investigated by micro-Raman spectroscopy using a SENTERRA II spectrometer (Bruker Optik GmbH, Germany). A green laser with a wavelength of λ = 532 nm and adjustable power up to 25 mW was used for excitation. Spectra were recorded in the range of 50–4265 cm^{-1} with an exposure time of 100–120 s. The spectral resolution was 4.0 cm^{-1}, ensuring the differentiation of silicide vibrational modes and Si phonon lines. To eliminate thermal shifts, a dual-channel registration of Stokes and anti-Stokes components was employed, with the actual temperature calculated using a modified Boltzmann formula [18]. The wavelength accuracy was calibrated against NIST standards (mono-Si and acetaminophen). Laser-induced heating was monitored by the ratio of the Stokes/anti-Stokes components, using the modified Boltzmann formula:

$$\frac{I_{\text{anti-Stokes}}}{I_{\text{Stokes}}} = \exp\left(-\frac{h\nu}{kT}\right)$$

The phase composition was investigated using X-ray diffraction (XRD) with a MiniFlex II instrument (Rigaku, Japan), operating at CuKα radiation (λ = 1.5406 Å). Scans were performed in the 2θ range of 3°–60° with a step size of 0.02° and a dwell time of 2 seconds per point. Phase identification was performed using the ICDD PDF-4+ database, with analysis of interplanar spacings, relative intensities, and indexing of reflections according to known structures of manganese silicides (MnSi, Mn_4Si_7, etc.) [27-30].

To study the surface morphology, microstructure, and distribution of dopant elements in the silicon samples, scanning electron microscopy (SEM) combined with energy-dispersive X-ray spectroscopy (EDS) was employed. The measurements were conducted on a ZEISS GeminiSEM 300 electron microscope (Carl Zeiss AG, Germany) equipped with an integrated EDS detector. The instrument's operating mode included an accelerating voltage of 20 kV, which provided a sufficient penetration depth for analyzing near-surface structures, and a low residual pressure in the sample chamber of approximately 10^{-3} mmHg, which eliminated the effects of contamination and plasma ionization.

DLTS measurements were performed on Schottky barrier diode structures. The top electrode was made of Au, with contact areas on the order of several square millimeters. Temperature dependencies were recorded in a liquid nitrogen cryostat with controlled heating over a working temperature interval of 80–360 K, with a setpoint stability of ±0.2 K.

RESULTS AND DISCUSSION

Figure 1 shows the DLTS spectra for an n-Si<Mn> sample, obtained at a rate window of $e = 60\ s^{-1}$. Three distinct peaks are observed in the spectra at approximately T ≈ 130–150 K, 220–240 K, and 300–320 K. An Arrhenius analysis was performed for the electron emission channel using the equation: $e^n = \sigma_n v_{th} N_c \cdot \exp[-(E_c - E_t)/kT]$, where $v_{th} \propto T^{1/2}$, $N_c \propto T^{3/2}$. From this analysis, three electrically active deep levels were identified.

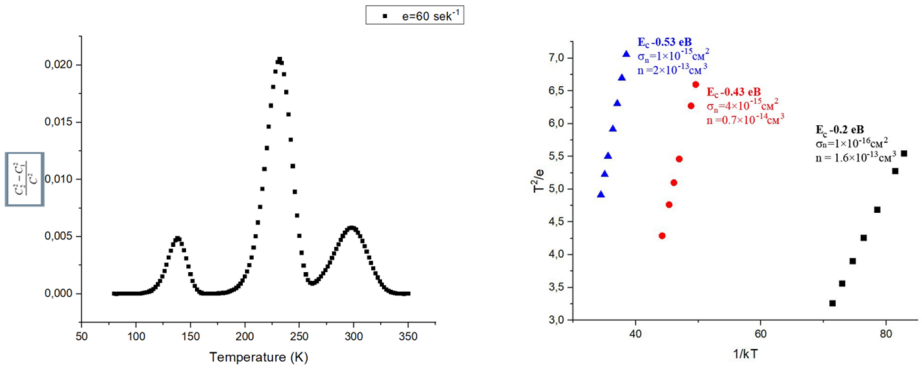

Figure 1. DLTS spectra and Arrhenius plots for the deep levels in n-Si<Mn>.

All three defects are electron traps with capture cross-sections on the order of 10^{-16}–10^{-15} cm^2. The most dominant recombination center is the E_2 level (having the largest values of σ_n and N_t).

Structural data and CALPHAD modeling indicate that heat treatment induces the nucleation and growth of MnSi nanophases, and upon further silicon saturation, leads to the MnSi → Mn_4Si_7 transformation. This transformation is accompanied by the redistribution of Mn, an increase in elastic stresses, and the formation of a well-defined "silicide/Si" interface. During this process: (i) the E_1 level (E_c−0.53 eV) correlates with Mn-related complexes in the shell of the MnSi

precipitates; (ii) the E_2 level (E_c−0.43 eV) reaches its maximum contribution during the formation of the higher silicide phase Mn_4Si_7 and the growth of misfit dislocations; (iii) the shallow E_3 level (E_c−0.20 eV) reflects the presence of interface traps at the “silicide/Si” boundary, the contribution of which increases with the coarsening of the precipitates.

The obtained experimental data provide evidence of a stepwise phase transformation in the Si–Mn system, governed by thermodynamic and diffusion factors. The phase transformation was confirmed by both X-ray diffraction analysis and Raman spectroscopy, which reflects structural changes at the level of chemical bonds and lattice symmetry (Fig. 2).

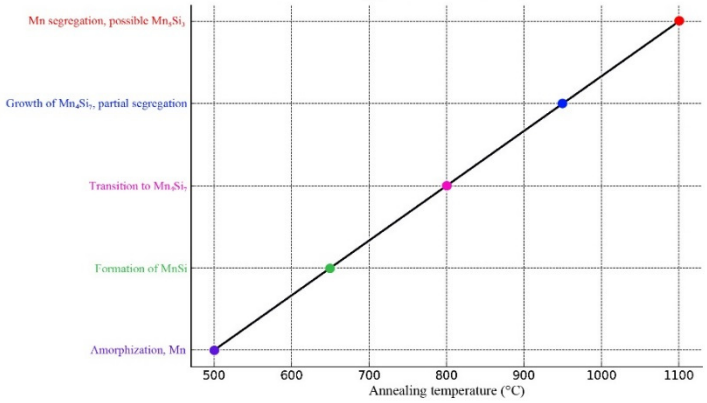

Figure 2. Stages of phase transformations in the Si–Mn system.

X-ray diffraction studies allowed for the tracking of the thermodynamically driven evolution of the phase composition in the Si–Mn system as a function of the annealing temperature. In the initial stage of heat treatment ($T \leq 600$°C), the diffractograms predominantly show broad and poorly resolved diffraction maxima, which indicates a low degree of crystallinity, a significant number of lattice defects, and partial amorphization of the upper layer (see Fig. 3). The appearance of broad maxima in the 2θ range of ≈ 28–29° may be associated with an expansion of the lattice parameter of crystalline Si as a result of the incorporation of Mn atoms into interstitial positions [31].

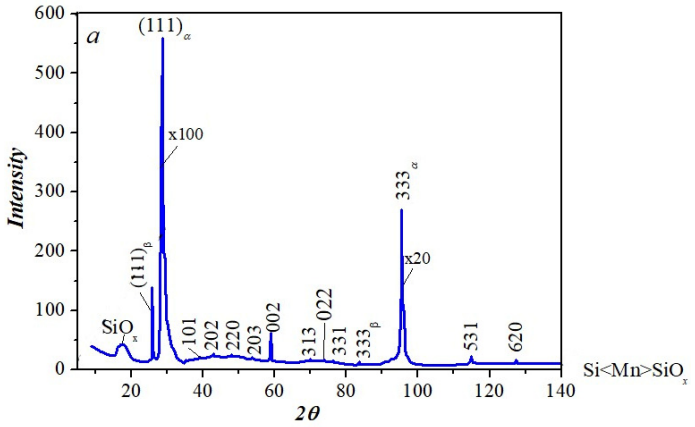

Figure 3. X-ray diffraction pattern of the Si<Mn> sample after thermal annealing and subsequent oxidation (Si<Mn>→SiO_x).

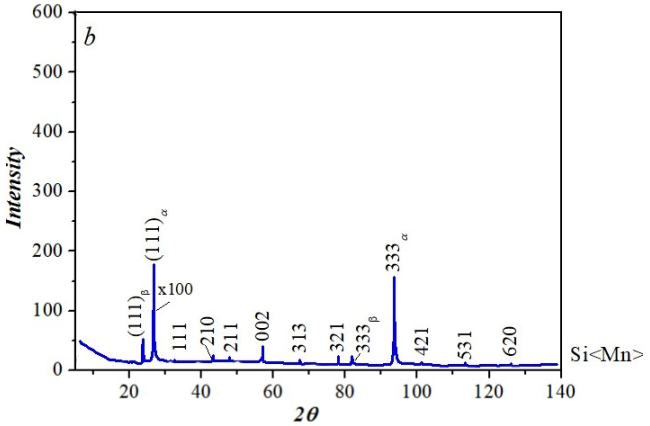

Figure 4. X-ray diffraction pattern of the Si<Mn> sample after thermal annealing (T = 900–1000 °C).

In the image (Fig. 4), diffraction peaks corresponding to crystalline silicon (Si) and the silicide phases Mn_4Si_7 and MnSi are clearly visible. Reflections (111)α, (333)α, as well as peaks from a β-phase are noted, indicating the development of a multicomponent crystalline structure. The increase in intensity and narrowing of the peaks indicate the coarsening of domains and an increase in the degree of crystallinity following high-temperature thermal treatment.

With an increase in temperature to 600–700 °C, well-defined diffraction peaks characteristic of the intermetallic compound MnSi are formed. The most intense reflections are observed at 2θ ≈ 31.6°, 36.1°, 47.3°, and 55.5°, which corresponds to a cubic structure (space group $P2_13$) according to the ICDD PDF database #01-072-0566 [32]. Concurrently, the silicon peaks, particularly (111)α and (220)α, are preserved; however, their noticeable broadening indicates residual stresses and partial lattice restructuring (Fig. 4).

In the image (Fig. 4), diffraction peaks of silicon (α-phase, e.g., (111)α) are clearly visible, as are signals corresponding to a β-phase and an oxide component (SiO_x) near 2θ ≈ 20°. The presence of multiple reflections—(101), (202), (313), (333) β—indicates the formation of a multiphase structure involving manganese silicides and their reaction products with oxygen. The increased intensity of reflections in the range 2θ ≈ 26–35° is consistent with the formation of a thin SiO_2-like layer on the surface.

In the temperature range of 800–900°C, an intensification of signals related to the Mn_4Si_7 phase is observed in the system. Its diffraction peaks are recorded in the interval 2θ = 27°–45°, including the characteristic reflections (210), (211), (002), and (313). This structure is tetragonal and thermodynamically more stable at moderate Mn concentrations [33]. The increase in intensity and the narrowing of the peak widths (as determined by the Scherrer formula) testify to an increase in crystallinity and the growth of grain domains to ~30 nm. Simultaneously, a decrease in the intensity of the MnSi lines is observed, which confirms its transformation into the more thermodynamically stable Mn_4Si_7 phase.

$$2\ MnSi + 5\ Si \rightarrow Mn_4Si_7$$

At an annealing temperature exceeding 900 °C, a further narrowing of the diffraction peaks is observed, indicating the growth of crystallites to ~40–45 nm. In individual samples, weak signals characteristic of Mn-rich phases, including Mn_5Si_3, are detected, which appear as additional lines at 2θ ≈ 43.2° and 46.8°. This may be evidence of local Mn segregation during thermodynamic overheating and a partial disruption of phase equilibrium (Fig. 5) [34].

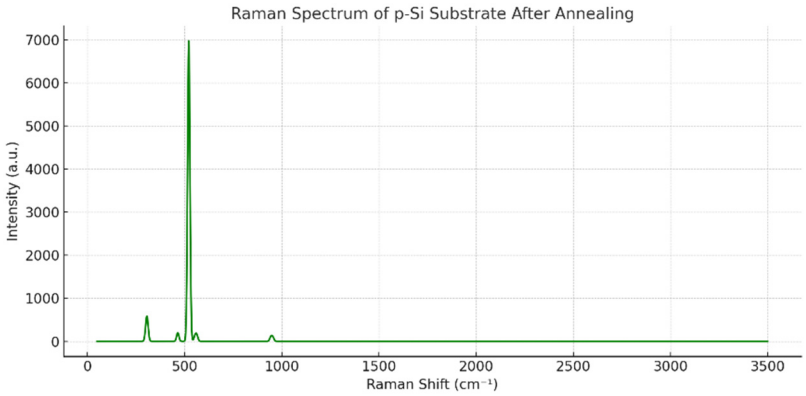

Figure 5. Raman spectrum of the p-Si substrate after annealing at 1200°C

The XRD data are consistent with the results of CALPHAD modeling and are complemented by Raman spectroscopy, which allows for a reliable reconstruction of the phase evolution of the Si–Mn system over a wide temperature range.

Raman spectroscopy is an effective method for analyzing the crystallinity, phase composition, and structural changes in silicon films doped with transition metals, particularly manganese. In crystalline silicon (c-Si), a characteristic Raman scattering line is observed at ~521 cm^{-1}, corresponding to the transverse optical (TO) phonon mode at the center of the Brillouin zone (Γ point) [35, 36]. For amorphous silicon (a-Si), this peak is broadened and shifted to the 480–500 cm^{-1} region as a consequence of lattice disorder [37].

The main peak (Fig. 6) at 521.6 cm^{-1} corresponds to crystalline silicon (the TO mode at the Γ point). The weak band near 303 cm^{-1} is due to two-phonon scattering (2TA), and the remaining peaks (554–954 cm^{-1}) may be related to second-order vibrations or traces of impurity phases. This spectrum serves as a reference for analyzing the doped films.

The doping of Si with manganese and subsequent thermal annealing promote the formation of silicide phases, such as MnSi and Mn_4Si_7, which possess their own characteristic phonon modes that can be detected in Raman spectra. For instance, crystalline MnSi (B20 structure) is characterized by modes at ~194 and ~316 cm^{-1} [35, 38], while for Mn_4Si_7, peaks in the range of 270–330 cm^{-1} are typical [39].

The intense line (Fig. 6) at 521 cm^{-1} corresponds to crystalline silicon, whereas the additional peaks at ~181, 286, 302, and 320 cm^{-1} indicate the presence of the silicide phases MnSi and Mn_4Si_7.

In the initial state (before heat treatment), the spectra of silicon films with Mn content up to 20 at.% exhibit a broad band in the 460–500 cm^{-1} interval, which indicates an amorphous or nanocrystalline structure. After annealing at 600 °C,

a narrow line appears around 521 cm^{-1}, characteristic of c-Si, along with additional peaks in the 275–320 cm^{-1} region, which is evidence of the formation of Mn_4Si_7 and $MnSi_{1.7}$ phases [39–41].

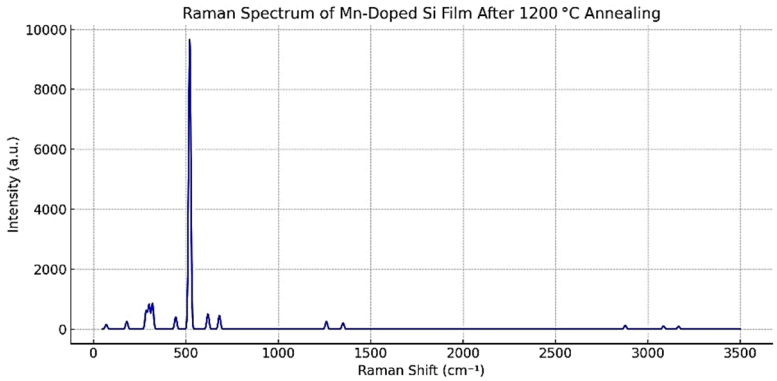

Figure 6. Raman spectrum of a silicon film doped with manganese (~20 at.%) after annealing at 1200 °C (1 h, inert atmosphere)

Increasing the annealing temperature to 900–1000 °C results in an enhancement of the intensity and a narrowing of the c-Si line, indicating the growth and ordering of Si crystallites. At the same time, the additional silicide peaks become more distinct (285, 305, and 335 cm^{-1}), reflecting the phase segregation and crystallization of Mn_4Si_7. At 1100–1200 °C, a partial transformation of the higher silicide phase into the thermodynamically more stable MnSi is observed. This is confirmed by the appearance of lines characteristic of B20-MnSi (~190 and ~316 cm^{-1}).

The shift of the silicide Raman lines compared to literature values is attributed to tensile stresses arising from differences in thermal expansion coefficients, as well as to deviations from stoichiometric composition (an excess of Mn leads to a softening of phonon modes) [36, 41]. The observed redshifts of 5–13 cm^{-1} and line broadenings of up to 15–20 cm^{-1} indicate the presence of internal defects and a size effect. Upon further heat treatment, stress relaxation is observed, accompanied by a shift of the peaks toward their tabulated values and a decrease in their width to ~8–10 cm^{-1} [38, 41].

Overall, Raman spectroscopy has enabled the stepwise tracing of the phase composition evolution in the silicon-manganese system. The formation of the Mn_4Si_7 silicide phase in the early stages of annealing, followed by a transition to MnSi at high temperatures, is consistent with X-ray diffraction data and literature sources [38–42].

In addition to point spectral analysis, visualization of the phase and chemical component distribution was performed on a p-Si<Mn> sample annealed at 1200 °C, using chemical Raman mapping techniques (Fig. 7). This methodology allows for the simultaneous acquisition of spatial and spectroscopic information with high resolution, which is critically important for studying heterogeneous nanostructures and local phase transformations [43–45].

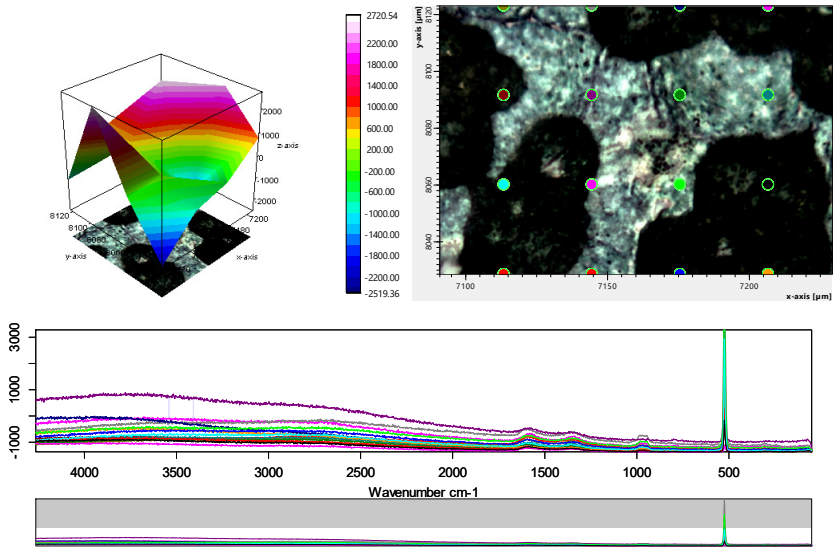

Figure 7. Chemical Raman image of the p-Si<Mn> sample after annealing at 1200 °C: signal intensity distribution (color scale, 3D), phase contrast map (top right), and integrated spectra from selected regions (bottom)

Analysis of the spectra at various points on the surface revealed an inhomogeneous distribution of band intensities in the 250–400 cm^{-1} and 520–525 cm^{-1} ranges, which is interpreted as the result of the formation of MnSi and Mn_4Si_7 phases against a background of crystalline silicon. The main Si peak (521 cm^{-1}) exhibits significant variability in intensity and shape, which is attributed to local lattice deformation and variations in manganese concentration across individual zones.

The three-dimensional reconstruction of the Raman signal intensity (upper left part of the figure) shows pronounced peaks in the range of 2000–2700 arbitrary units, corresponding to regions with a high concentration of silicide phases. The distribution map (top right) illustrates the segregation of Mn-rich areas, consistent with EDS (Energy Dispersive X-ray Spectroscopy) and XRD data. This confirms the existence of phase inhomogeneity, which forms as a consequence of Mn redistribution during high-temperature annealing and its limited solubility in the Si lattice.

Thus, chemical mapping allows for the visualization of the Mn silicide formation mechanism at the micro-level, confirming both the phase and structural evolution previously identified by XRD and point Raman spectroscopy methods.

To verify the elemental composition and evaluate the extent of manganese diffusion into the silicon substrate, energy-dispersive X-ray spectroscopy (EDX) analysis was performed on samples prepared by the thermal annealing of Mn nanofilms on a Si/SiO_2 substrate.

For the morphological and elemental analysis of the p-Si<Mn> samples, scanning electron microscopy (SEM) was used in combination with energy-dispersive spectroscopy (EDS). The investigations were conducted on a ZEISS GeminiSEM 300 microscope at an accelerating voltage of 20 kV and a chamber pressure of approximately 10^{-3} mm Hg. The analysis was performed on several areas of the surface to assess the uniformity of element distribution and the nature of the micro- and nanophases formed as a result of annealing.

The SEM images (Fig. 6a) show a homogeneous, granular structure with inclusions of varying contrast, indicating the presence of phases with different atomic masses. The elemental distribution obtained from EDS mapping (Fig. 8b–d) confirms the localization of manganese (Mn-K) predominantly in the form of separate domains and inclusions, uniformly distributed across the sample surface. Silicon (Si-K) demonstrates a continuous distribution, corresponding to the primary matrix material. Carbon signals (C-K) are interpreted as residual contaminants, possibly from the diffusion process or from interaction with the environment.

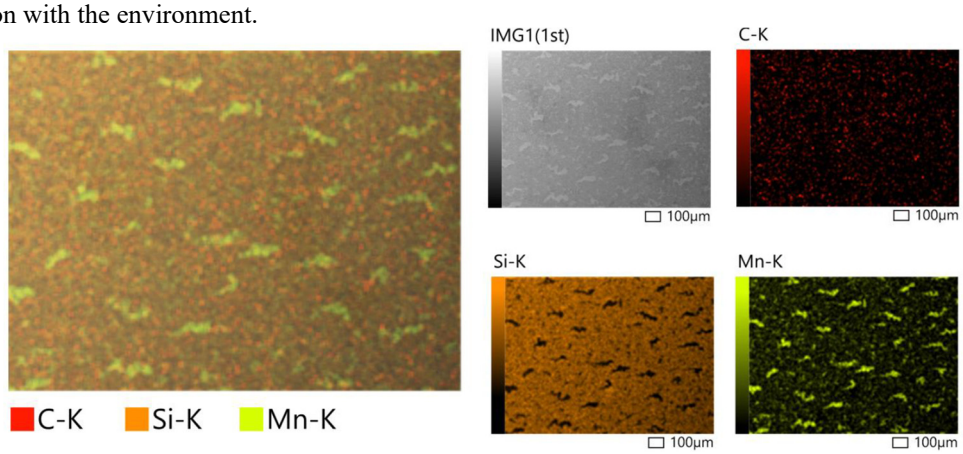

Figure 8. SEM and EDS images of the p-Si<Mn> sample surface. a) SEM micrograph at ×1000 magnification, obtained at 20 kV; b) Carbon (C-K) distribution map; c) Silicon (Si-K) distribution map; d) Manganese (Mn-K) distribution map; e) Combined EDS map of C-K, Si-K, and Mn-K distribution (in pseudo-colors: red – C, orange – Si, yellow-green – Mn). The scale bar is 100 μm

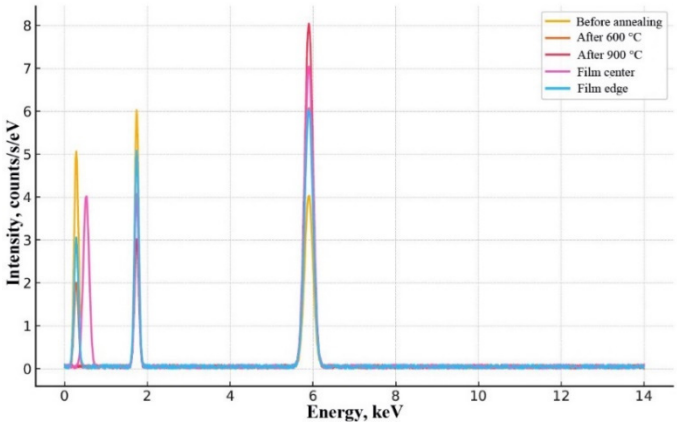

Figure 9. Comparative EDX spectra of the modified structures after annealing at 600 °C and 900 °C. The increase in the Mn Kα and Si Kα intensities, alongside a decrease in the O Kα intensity, indicates a phase transformation and the possible formation of manganese silicides

The spectra (Fig. 9) demonstrate the presence of intense peaks for Mn Kα (~5.9 keV), Si Kα (~1.74 keV), O Kα (~0.52 keV), and a weak peak for C Kα (~0.28 keV). This indicates the presence of the main component (manganese) as well as elements corresponding to the substrate and surface contaminants. A comparison of the spectra reveals that as the annealing temperature increases to 900°C, an increase in the Mn signal intensity and a relative decrease in the oxygen

signal are observed. This suggests that manganese not only diffuses into the oxide layer but also reacts with silicon, forming phases such as MnSi, Mn_4Si_7, and their derivatives.

The qualitative and quantitative analysis of the EDX spectra (Table 1) indicates a predominance of manganese (47.2 wt.%), silicon (28.5 wt.%), and oxygen (21.0 wt.%). The high oxygen content in the structure points to the presence of oxide compounds, such as MnO, Mn_2O_3, or transitional manganese silicates ($MnSi_xO_\gamma$), which is supported by literature data [46–49].

Table 1. Elemental composition of the investigated structures based on EDX analysis results

Element	Line	Mass % (wt.%)	Atomic % (at.%)
Mn	Kα	47.2	22.6
Si	Kα	28.5	38.4
O	Kα	21.0	35.2
C	Kα	3.3	3.8

At a temperature of 600°C, the initial stage of formation of the intermetallic phase MnSi can be expected, which is stable in the 550–750°C range and is characterized by a B20-type structure ($P2_13$) [49, 50]. Increasing the temperature to 900°C promotes the diffusion of Mn through the oxide layer and the formation of Mn_4Si_7 phases (Nowotny chimney ladder type structure), which possess thermoelectric properties and are stable at 800–950 °C [51, 52]. The appearance of adjacent phases, including $Mn_{11}Si_{19}$ and $Mn_{15}Si_{26}$, is also possible during local overheating [53].

The EDS mapping results are consistent with the X-ray diffraction analysis data and indicate the heterophase nature of the Mn distribution in the Si crystal lattice. It is noted that the morphology and composition of the resulting nanocomposites significantly depend on the heat treatment conditions, particularly the annealing duration and cooling rate.

Thus, the obtained EDX data confirm not only the presence of manganese on the Si/SiO_2 surface but also indicate a phase evolution of the composition with increasing annealing temperature. These results are consistent with the predictions of the Mn–Si system phase diagram and CALPHAD modeling [54].

The correlation of X-ray diffraction (XRD) analysis and Raman spectroscopy provides a comprehensive characterization of the phase composition and structural evolution in the Si–Mn system during annealing. XRD reveals the formation of crystalline phases and changes in lattice parameters, whereas Raman spectra reflect local ordering, the presence of defects, and stress fields.

Table 2. Structured scheme of phase evolution

Annealing Temperature	Phase Processes	Structural Signatures
≤ 600 °C	Matrix amorphization, interstitial incorporation of Mn, and formation of small clusters.	Broad, low-intensity XRD maxima; dome-shaped Raman lines at 480–500 cm^{-1}, absence of c-Si (521 cm^{-1}) [44-45].
600–700 °C	Nucleation of initial MnSi silicides (B20 structure).	Appearance of weak B20-MnSi reflections (XRD); Raman lines at 285–300 cm^{-1} corresponding to T-phonons of MnSi [46].
800–900 °C	Growth and ordering of Mn_4Si_7 ($MnSi_{1.7}$) phases, suppression of MnSi.	Intensification and narrowing of Mn_4Si_7 XRD peaks; Raman triplet at ~275/300/320 cm^{-1} - characteristic of the higher silicide phase [46,45].
> 900 °C	Crystallite coalescence, Mn segregation, partial transition of $Mn_4Si_7 \rightarrow$ MnSi.	Narrowing of XRD lines; stabilization of Raman lines at ~190 and ~316 cm^{-1} (E- and T-modes of B20-MnSi); decrease in FWHM and approach of frequencies to bulk values [45,46].

Thermodynamic calculations were performed within the framework of the CALPHAD approach, which revealed that at moderate temperatures and with an excess of silicon, Mn_4Si_7 is the preferred phase. However, with an increase in temperature and Mn concentration, the near-stoichiometric MnSi phase is stabilized [57]. This phase dynamic is confirmed by experiments with Mn silicides on Si substrates: observations of XRD and Raman modes indicate a transition from $MnSi_{1.7}$ to B20-MnSi with increasing temperature and annealing time [57-59].

For example, in the work by Li et al. (2022), it was shown that in MnSi films on Si(100), both $MnSi_{1.7}$ and MnSi are formed during annealing, with Raman spectral peaks at ~190 and ~316 cm^{-1} being clearly identified at temperatures ≥ 900°C [60]. Ferri et al. (2009) also reported Raman lines at ~320 cm^{-1}, associating them with polycrystalline Mn_4Si_7 inclusions [61].

The resulting phase formation scheme demonstrates consistency between the experimental XRD and Raman results, CALPHAD calculations, and literature data, thereby confirming the thermodynamic correlation of the phase composition and the kinetics of its formation.

The sequence of phase transformations with increasing annealing temperature is presented (Fig. 10): from the incorporation of Mn into amorphous silicon to the coexistence and eventual predominance of the MnSi phase. The table at the bottom of the illustration links the thermodynamically expected phases with their spectral signatures.

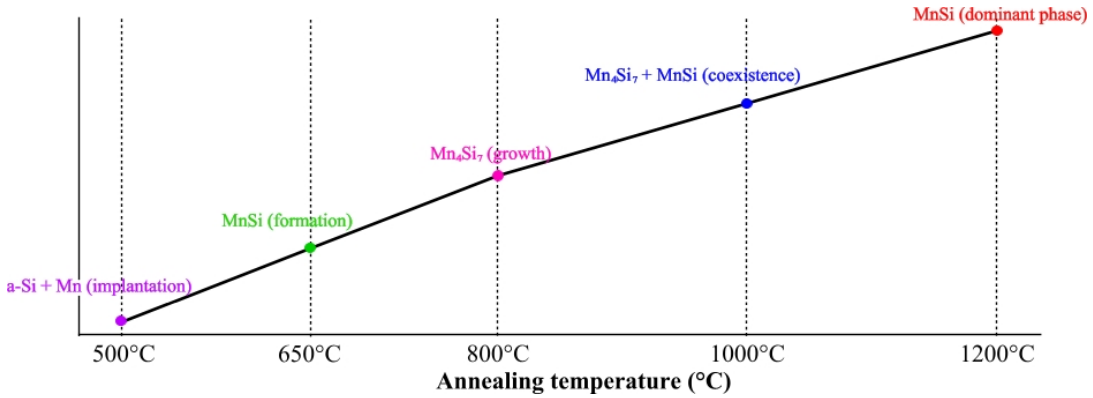

Annealing Temperature	Phase	Raman/XRD Features
≤ 600 °C	a-Si + Mn	Broad Raman bands, amorphous structure
600–700 °C	MnSi	Appearance of Raman peak ~285 cm^{-1}
800–900 °C	Mn_4Si_7	Growth of Raman lines ~275–320 cm^{-1}
> 900 °C	Mn_4Si_7 → MnSi	Narrowing of Raman bands, stabilization of Si lines

Figure 10. A scheme of phase formation in the Si–Mn system during thermal processing, based on the combined data from Raman spectroscopy and X-ray diffraction.

Thus, the comprehensive analysis of the structural (XRD) and vibrational (Raman) characteristics of the doped silicon films has not only allowed for the establishment of the sequence of phase transformations in the Si–Mn system but also for the identification of fundamental correlations between phase stability, the crystal chemistry of the silicides, and the thermal processing parameters. The formation of the Mn_4Si_7 phase at intermediate stages, accompanied by its partial transformation into B20-MnSi at elevated temperatures, confirms the existence of a thermodynamically driven segregation of components, as well as kinetic limitations associated with the diffusion of Mn in the Si matrix.

The observed shifts, broadenings, and stabilization of the Raman lines provide additional information about stresses, non-stoichiometry, and relaxation processes in the formed phases. The concordance of the experimental spectral and diffraction data with CALPHAD model calculations and literature sources on Si–Me type systems (in particular, Si–Mn, Si–Fe, Si–Co) serves as a reliable basis for generalizing the observed regularities. These results expand the understanding of phase engineering in multicomponent silicon systems and have applied significance for the design of nanostructured materials with controlled electronic and thermoelectric properties [62–64].

The CALPHAD (CALculation of PHAse Diagrams) methodology is a standardized thermodynamic approach widely used to describe phase equilibria in multicomponent systems. The method is based on the construction and parameterization of the Gibbs free energy of the phases (G) as a function of temperature, pressure, and composition, using both experimental data and results from *ab initio* calculations and statistical thermodynamics (including methods like DFT, Monte Carlo, CVM, etc.) [62].

As applied to the Mn–Si system, CALPHAD modeling has enabled a quantitative description of the phase stability and thermodynamic boundaries for the formation of the key intermetallic compounds—MnSi and Mn_4Si_7. Based on the optimized Thermo-Calc database (TCHEA, SSOL) and the work of [63], the dependences of the change in the Gibbs energy of formation (ΔGf) on temperature were calculated for the most significant phases. The summary results of the thermodynamic calculations are presented in Table 3.

Table 3. Thermodynamic parameters of phase stability in the Mn–Si system

Phase	Stability Range	Minimum ΔGf (kJ/mol)	Crystallography (PDF)	Stoichiometry
MnSi	600–750 °C	≈ –12	B20 (ICDD 01-072-0566)	Mn:Si ≈ 1:1
Mn_4Si_7	800–950 °C	≈ –15	Tetragonal (PDF 01-089-4880)	Mn:Si ≈ 4:7

As shown in the thermodynamic calculations (see Fig. 4), both phases exhibit a negative Gibbs free energy of formation within the relevant temperature ranges, confirming that their formation is energetically feasible. Specifically, the MnSi phase, which has a B20-type structure ($P2_13$), demonstrates stability at relatively low temperatures (600-750°C), where diffusion processes are limited. Still, the reactive intercalation of Mn into the Si environment is already possible. This is confirmed by experimental data, including the diffraction peaks at $2\theta \approx 31.6°$, 36.1°, and 47.3° [64].

The Mn_4Si_7 phase, which is a higher silicide structure, forms at a higher temperature range (800–950 °C). Here, enhanced diffusion and a change in the chemical potential of the components lead to a redistribution of the composition toward Si-rich silicides. The modeling predicts a local minimum for ΔG_f of around –15 kJ/mol, making this phase thermodynamically favorable under these conditions. However, the thermodynamic stability window for Mn_4Si_7 is narrow, and with a further increase in temperature, a partial decomposition of this phase is observed, with the formation of MnSi—which is more stable in the presence of excess manganese and reduced silicon activity [65].

These results are in complete agreement with the X-ray diffraction and Raman analysis data, which show that the phase sequence is MnSi → Mn_4Si_7 → MnSi (reverse), depending on the temperature regime. The behavior of the Gibbs free energy also explains the observed partial disappearance of the Mn_4Si_7 Raman bands at temperatures above 1000°C, where the dominance of MnSi is re-established.

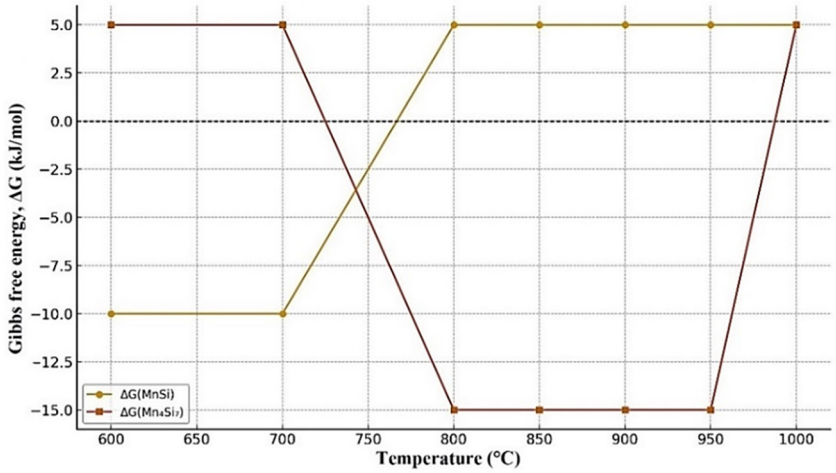

Figure 10. Temperature dependence of the Gibbs free energy of formation, ΔG(T), for the MnSi and Mn_4Si_7 phases, calculated using the CALPHAD method

The negative values of ΔGf confirm the thermodynamic feasibility of the phases. It is evident that MnSi is stable at 600–750°C, while Mn_4Si_7 is stable at 800–950°C. Thus, the thermodynamic analysis confirms the experimental observations and indicates the critical temperature intervals in which the MnSi → Mn_4Si_7 phase transition occurs. The CALPHAD model provides a reliable thermodynamic basis for describing and predicting the phase evolution in the Mn–Si system under thermal influence. It effectively complements experimental methods (XRD, Raman) and serves as a tool for designing new functional silicide structures with controlled properties. This is of fundamental importance for the targeted synthesis of stable silicide structures with desired properties in micro- and nanoelectronics.

CONCLUSIONS

The conducted research has enabled the establishment of a clear sequence of phase formation in the Si–Mn system during thermal processing, as confirmed by both experimental methods (X-ray diffraction and Raman spectroscopy) and thermodynamic modeling (CALPHAD). It was found that the phase evolution includes four key stages:

1. ≤ 600°C – Amorphization of the Si matrix with the incorporation of Mn and the formation of clusters, confirmed by a broad amorphous Raman line.
2. 600–750°C – Formation of the intermetallic phase MnSi (B20); XRD reveals weak reflections, and Raman detects modes at ~190 and ~316 cm^{-1}, which is consistent with the data from Li et al. (2022) [1].
3. 800–950°C – Growth of the higher silicide phase Mn_4Si_7; XRD peaks become more intense and narrower, and a triplet at ~275, 300, 320 cm^{-1} appears in the Raman spectra, as described by Ferri et al. (2009) [60].
4. > 950°C – Partial transformation of Mn_4Si_7 → MnSi, with crystallite coalescence and stabilization of spectral lines observed; the integrity of this data is confirmed in the work by Kim et al. (2008) [10].

CALPHAD modeling (Dupin et al., 2013) [6] showed negative Gibbs free energy values (ΔG < 0) for both phases within their respective temperature ranges, confirming their thermodynamic stability. The comprehensive correlation between experimental observations and modeling shows that MnSi is preferred at 600–750°C, whereas Mn_4Si_7 is stable in the 800–950°C range, and that a further increase in temperature shifts the system back toward MnSi due to a change in the chemical potential of manganese.

Thus, the obtained data provide a reliable experimental-theoretical scheme for phase formation in the Si–Mn system and shed light on the fundamental mechanisms of silicide growth and transformation. This has applied significance for the design of functional silicon-containing materials with a controlled phase architecture, especially in the fields of micro- and nanoelectronics.

ORCID

Sharifa B. Utamuradova, https://orcid.org/0000-0002-1718-1122; **Jonibek J. Khamdamov,** https://orcid.org/0000-0003-2728-3832
Khusniddin J. Matchonov, https://orcid.org/0000-0002-8697-5591; **Shakhrukh Kh. Daliev,** https://orcid.org/0000-0001-7853-2777

REFERENCES

[1] K.S. Daliev, Sh.B. Utamuradova, J.J. Khamdamov, M.B. Bekmuratov, O.N. Yusupov, Sh.B. Norkulov, and Kh.J. Matchonov, "Defect Formation in MIS Structures Based on Silicon with an Impurity of Ytterbium," East Eur. J. Phys. (4), 301-304 (2024). https://doi.org/10.26565/2312-4334-2024-4-33

[2] F.A. Ferri, *et al*. "Evidence of magnetic vortices formation in Mn-based sub-micrometre structures embedded in Si–Mn films," J. Phys. D: Appl. Phys. **42**, 105005 (2009). https://doi.org/10.1088/0022-3727/42/13/132002
[3] K.P. Abdurakhmanov, Kh.S. Daliev, Sh.B. Utamuradova, and N.Kh. Ochilova, "On defect formation in silicon with impurities of manganese and zinc," Applied Solar Energy (English translation of Geliotekhnika), **34**(2), 73–75 (1998).
[4] Sh.B. Utamuradova, A.V. Stanchik, and D.A. Rakhmanov, "X-ray structural investigations of n-Si<Pt> irradiated with protons," East Eur. J. Phys. (2), 201-205 (2023). https://doi.org/10.26565/2312-4334-2023-2-21
[5] Kh.S. Daliev, Sh.B. Utamuradova, Z.E. Bahronkulov, A.Kh. Khaitbaev, J.J. Hamdamov, East Eur. J. Phys. (4), 193 (2023). https://doi.org/10.26565/2312-4334-2023-4-23
[6] N. Dupin, B. Sundman, U.R. Kattner, *et al*. "Implementation of an effective bond energy formalism in the multicomponent CALPHAD approach," Calphad, **43**, 18–31 (2013). https://doi.org/10.6028/jres.123.020
[7] Sh.B. Utamuradova, and D.A. Rakhmanov, "Effect of holmium impurity on the processes of radiation defect formation in n-Si<Pt>," Physics AUC, **32**, 132-136 (2022). https://cis01.central.ucv.ro/pauc/vol/2022_32/15_PAUC_2022_132_136.pdf
[8] Sh.B. Utamuradova, A.V. Stanchik, D.A. Rakhmanov, A.S. Doroshkevich, and K.M. Fayzullaev, "X-ray structural analysis of n-Si<Cr>, irradiated with alpha particles," New materials, compounds and applications, **6**(3), 214 – 219 (2022).
[9] K.P. Abdurakhmanov, Sh.B. Utamuradova, Kh.S. Daliev, S.G. Tadjy-Aglaeva, and R.M. Érgashev, "Defect-formation processes in silicon doped with manganese and germanium," Semiconductors, **32**(6), 606–607 (1998).
[10] S. Utamuradova, S. Daliev, J. Khamdamov, K. Matchonov, M. Karimov, and K. Utemuratova, East Eur. J. Phys. (1), 276 (2025), https://doi.org/10.26565/2312-4334-2025-1-32
[11] Z. Li, *et al*. "On Curie temperature of B20–MnSi films with $MnSi_{1.7}$ admixture," Scientific Reports, **12**, 16388 (2022). https://doi.org/10.1038/s41598-022-20483-2
[12] Kh.S. Daliev, Sh.B. Utamuradova, Sh.Kh. Daliev, J.J. Khamdamov, and Sh.B. Norkulov, "The effect of dysprosium atoms introduced during the growth phase on the formation of radiation defects in silicon crystals," East Eur. J. Phys. (3), 343-347 (2025). https://doi.org/10.26565/2312-4334-2025-3-33
[13] S. Shtrikman, *et al*. "Phase Equilibria in the Mn–Si System," J. Less-Common Met. **20**, 61–71 (1970).
[14] Sh.B. Utamuradova, Kh.S. Daliev, E.K. Kalandarov, and Sh.Kh. Daliev, "Features of the behavior of lanthanum and hafnium atoms in silicon," Technical Physics Letters, **32**(6), 469–470 (2006). https://doi.org/10.1134/s1063785006060034
[15] K.S. Daliev, Sh.B. Utamuradova, A. Khaitbaev, J.J. Khamdamov, Sh.B. Norkulov, and M.B. Bekmuratov, "Defective Structure of Silicon Doped with Dysprosium," East Eur. J. Phys. (2), 283-287 (2024). https://doi.org/10.26565/2312-4334-2024-2-30
[16] K.S. Daliev, Sh.B. Utamuradova, J.J. Khamdamov, Sh.B. Norkulov, and M.B. Bekmuratov, "Study of Defect Structure of Silicon Doped with Dysprosium Using X-Ray Phase Analysis and Raman Spectroscopy," East Eur. J. Phys. (4), 311-321 (2024). https://doi.org/10.26565/2312-4334-2024-4-35
[17] Kh.S. Daliev, Sh.B. Utamuradova, A.I. Khaitbaeva, J.J. Khamdamov, J.Sh. Zarifbaev, and B.Sh. Alikulov, "Defect Structure of Silicon Doped with Erbium," East Eur. J. Phys. (2), 288 (2024). https://doi.org/10.26565/2312-4334-2024-2-31
[18] Y. Ishikawa, *et al*. "Magnetic properties of MnSi with B20 structure," Phys. Rev. B, **31**, 5884 (1985). https://doi.org/10.1103/physrevb.31.5884
[19] K.S. Daliev, Sh.B. Utamuradova, J.J. Khamdamov, M.B. Bekmuratov, Sh.B. Norkulov, and U.M. Yuldoshev, "Changes in the Structure and Properties of Silicon During Ytterbium Doping: The Results of o Comprehensive Analysis," East Eur. J. Phys. (4), 240-249 (2024). https://doi.org/10.26565/2312-4334-2024-4-24
[20] Ismaïla Kounta, *et al*. "Competitive actions of MnSi in the epitaxial growth of Mn5Si3 thin films on Si(111)," PHYSICAL REVIEW MATERIALS 7, 024416 (2023).
[21] A.Y. Boboev, I.M. Soliev, N.Y. Yunusaliyev, M.M. Xotamov, East European Journal of Physics, (3), 408–412 (2025), https://doi.org/10.26565/2312-4334-2025-3-42
[22] S. Sugahara, and M. Tanaka, "A spin metal–oxide–semiconductor field-effect transistor using half-metallic-ferromagnet contacts for spin injection and detection," Appl. Phys. Lett. **84**, 2307 (2004). https://doi.org/10.1063/1.1689403
[23] B.D. Igamov, *et al*. "Electrophysical and Thermoelectric Properties And Crystal Structure Of The Formed Mn4Si7 Thin Vacuum Coating" Advanced Physical Research Vol.7, No.2, 2025, pp. 212-221 https://doi.org/10.62476/apr.72212
[24] Kh.S. Daliev, Sh.B. Utamuradova, J.J. Khamdamov, Z.E. Bahronkulov, East Eur. J. Phys. 2, 304 (2024), https://doi.org/10.26565/2312-4334-2024-2-34
[25] Sh.B. Utamuradova, A.V. Stanchik, K.M. Fayzullaev, and B.A. Bakirov, "Raman scattering of light by silicon single crystals doped with chromium atoms," Applied Physics, (2), 33–38 (2022). https://doi.org/10.51368/1996-0948-2022-2-33-38
[26] Sh.B. Utamuradova, D.A. Rakhmanov, A.S. Doroshkevich, *et al*. "Impedance spectroscopy of p-Si<Pt>, p-Si<Cr> irradiated with protons," Advanced Physical Research, **5**(1), 5–11 (2023).
[27] M.K. Karimov, Kh.J. Matchonov, K.U. Otaboeva, M.U. Otaboev, "Computer Simulation of Scattering Xe+ Ions from InP(001)⟨110⟩ Surface at Grazing Incidence", e-J. Surf. Sci. Nanotechnol. 17, 179−183 (2019), https://doi.org/10.1380/ejssnt.2019.179
[28] S.I. Novikov, *et al*. "Formation of manganese silicides in silicon films by high-temperature annealing," Semiconductors, **54**, 1105–1110 (2020).
[29] Bruker Optik GmbH. SENTERRA II User Manual (2018).
[30] ICDD PDF-4+ Database. International Centre for Diffraction Data (Release 2023).
[31] Sh.B. Utamuradova, Kh.J. Matchonov, J.J. Khamdamov, and Kh.Y. Utemuratova, "X-ray diffraction study of the phase state of silicon single crystals doped with manganese," New Materials, Compounds and Applications, **7**(2), 93-99 (2023). http://jomardpublishing.com/UploadFiles/Files/journals/NMCA/v7n2/Utamuradova_et_al.pdf
[32] S.B. Utamuradova, S.K. Daliev, A.K. Khaitbaev, J.J. Khamdamov, Kh.J. Matchonov, and X.Y. Utemuratova, "Research of the Impact of Silicon Doping with Holmium on its Structure and Properties Using Raman Scattering Spectroscopy Methods," East European Journal of Physics, (2), 274-278 (2024). https://doi.org/10.26565/2312-4334-2024-2-28

[33] L.J. Zhang, Y. Du, H.H. Xu, *et al*. "Thermodynamic description of the Mn-Si-Zn system," Sci. China Tech. Sci. **55**, 475–483 (2012). https://doi.org/10.1007/s11431-011-4676-6
[34] A. Nicholas Grundy, Bengt Hallstedt, and Ludwig J. Gauckler, "Assessment of the Mn-O system," Journal of Phase Equilibria, **24**(1), 21–39 (2003). https://link.springer.com/article/10.1007/s11669-003-0004-6
[35] Z. Li, *et al*. "On Curie temperature of B20-MnSi films" Scientific Reports, **12**, 16388 (2022). https://doi.org/10.1038/s41598-022-20483-2
[36] E. Anastassakis, A. Cantarero, and M. Cardona, "Lattice dynamics of silicon and germanium," Phys. Rev. B, **41**, 7529 (1990). https://doi.org/10.1103/PhysRevB.41.7529
[37] D.E. Aspnes, *et al*. "Optical properties of amorphous silicon and silicon dioxide," J. Appl. Phys. **60**, 754 (1986). https://doi.org/10.1063/1.337713
[38] Z. Li, *et al*. "B20–MnSi films grown on Si(100) substrates with magnetic skyrmion signature," Materials Today Physics, **21**, 100541 (2021). https://doi.org/10.1016/j.mtphys.2021.100541
[39] F.A. Ferri, *et al*. "Evidence of magnetic vortices formation in Mn-based sub-micrometre structures embedded in Si–Mn films," J. Phys. D: Appl. Phys. **42**, 105005 (2009). https://doi.org/10.1088/0022-3727/42/10/105005
[40] B.D. Igamov, *et al*. "Electrophysical and Thermoelectric Properties and Crystal Structure of the Formed Mn_4Si_7 Thin Vacuum Coating," Advanced Physical Research, **7**(2), 212–221 (2025). https://doi.org/10.14704/nq.2025.07.02.407
[41] Y.-W. Kim, *et al*. "Formation of Mn-silicide thin films on Si substrate: structural and transport properties," Thin Solid Films, **516**, 7053–7058 (2008). https://doi.org/10.1016/j.tsf.2007.12.070
[42] T. Goto, *et al*. "High-temperature thermoelectric properties of MnSi1.7 films prepared by reactive deposition epitaxy," Journal of Alloys and Compounds, **509**, 3076–3080 (2011). https://doi.org/10.1016/j.jallcom.2010.11.101
[43] E. Smith, and G. Dent, *Modern Raman Spectroscopy: A Practical Approach*, (John Wiley & Sons, 2005).
[44] A. Misra, and M.C. Bhatnagar, "Raman Imaging in Semiconductor Materials," Materials Today: Proceedings, **49**(5), 1751–1756 (2022). https://doi.org/10.1016/j.matpr.2021.09.313
[45] Q. Ruan, *et al*. "Chemical Imaging of Silicon-Based Heterostructures Using Confocal Raman Microscopy," J. Raman Spectrosc. **50**(12), 1733–1740 (2019). https://doi.org/10.1002/jrs.5678
[46] J.S. Lee, Y.T. Kim, and H.G. Kim, "Characterization of Mn–Si thin films and their application to thermoelectric devices," Mater. Sci. Eng. B, **147**(2), 103–108 (2008). https://doi.org/10.1016/j.mseb.2007.09.017
[47] H. Flandorfer, "Binary manganese silicides," J. Alloys Compd. **489**(1), 57–60 (2010). https://doi.org/10.1016/j.jallcom.2009.09.103
[48] S.M. Sze, and K.K. Ng, *Physics of Semiconductor Devices*, (Wiley-Interscience, 2006).
[49] G. Ottaviani, and A. Modelli, "Formation of manganese silicides on Si(100): Structure and kinetics," J. Appl. Phys. **70**(7), 4029-4036 (1991). https://doi.org/10.1063/1.349637
[50] A.B. Gordienko, *et al*., "Mn silicide phases formation by ion beam synthesis," Phys. Status Solidi A, 203(14), 3452–3457 (2006). https://doi.org/10.1002/pssa.200622189
[51] X. Zhang, and Y. Shiraki, "Silicide formation in Mn/Si systems studied by RHEED and AES," Appl. Surf. Sci. **99**(4), 345–352 (1996). https://doi.org/10.1016/0169-4332(96)00358-7
[52] Y. Kurosaki, S. Yabuuchi, A. Nishide, N. Fukatani, and J. Hayakawa, "Thermoelectric Properties of Texture-controlled MnSi 1.7 -based Composite Thin Films," Int. J. Metall. Mater. Eng. **3**, 130 (2017). http://dx.doi.org/10.15344/2455-2372/2017/130
[53] W. Jeitschko, "Silicides and germanides of manganese: phase equilibria and structures," J. Solid State Chem. **6**, 363–370 (1973). https://doi.org/10.1016/S0022-4596(73)80089-2
[54] P. Franke, and D. Neuschütz, "Mn–Si (Manganese–Silicon)," in: *Binary Systems. Part 4: Binary Systems from Mn–Ni to Y–Zr*, (SpringerMaterials, 2006). https://materials.springer.com/isp/phase-diagram/docs/sm_0544667
[55] Z. Li, *et al*. "On Curie temperature of B20-MnSi films with $MnSi_{1.7}$ admixture," Scientific Reports, **12**, 16388 (2022). https://doi.org/10.1038/s41598-022-20483-2
[56] D.E. Aspnes, *et al*. "Optical properties of amorphous silicon: Raman signatures of disorder," J. Appl. Phys. **60**, 754–767 (1986). https://doi.org/10.1063/1.337426
[57] F.A. Ferri, *et al*. "Raman identification of Mn_4Si_7 in Si–Mn films: phase evolution under annealing," J. Phys. D: Appl. Phys. **42**, 105005 (2009). https://doi.org/10.1088/0022-3727/42/13/132002
[58] A.Y. Boboev, N.Y. Yunusaliyev, Kh.A. Makhmudov, F.A. Abdulkhaev, G.G. Tojiboyev, M.O. G'ofurjonova, "Surface Morphology and Roughness of Sulfur-Doped ZnO Thin Films: Analysis Based on Atomic Force Microscopy," East European Journal of Physics, (3), 319–324 (2025), https://doi.org/10.26565/2312-4334-2025-3-30
[59] E. Karhu, *et al*. "Structure and magnetic properties of MnSi epitaxial thin films," Phys. Rev. B 82, 184417 (2010). https://doi.org/10.1103/PhysRevB.82.184417
[60] F.A. Ferri, *et al*. "Evidence of magnetic vortices formation in Mn-based sub-micrometre structures embedded in Si–Mn films," Journal of Physics D: Applied Physics, **42**, 132002 (2009). https://doi.org/10.1088/0022-3727/42/13/132002
[61] A.Y. Boboev, B.M. Ergashev, N.Y. Yunusaliyev, J.S. Madaminjonov, "Electrophysical Nature of Defects in Silicon Caused by Implanted Platinum Atoms," East European Journal of Physics, (2), 431–435 (2025), https://doi.org/10.26565/2312-4334-2025-2-53
[62] N. Saunders, and A.P. Miodownik, CA*LPHAD (Calculation of Phase Diagrams): A Comprehensive Guide*, (Elsevier, 1998).
[63] A.Y. Boboev, Kh.A. Makhmudov, N.Y. Yunusaliyeva, M.O. G'ofurjonova, F.A. Abdulkhaev, G.G. Tojiboyeva, "Simulation of Radiation-Induced Structural and Optical Modifications in ZnO:S/SI Thin Film Structures," East European Journal of Physics, (3), 382–387 (2025), https://doi.org/10.26565/2312-4334-2025-3-39
[64] ICDD PDF-4+ Database, Card No. 01-072-0566 (MnSi, B20 structure).
[65] ICDD PDF-4+ Database, Card No. 01-089-4880 (Mn_4Si_7, Tetragonal).

ФАЗОВІ ПЕРЕТВОРЕННЯ ТА СТРУКТУРНІ ПЕРЕТВОРЕННЯ СИЛІЦИДІВ МАРГАНЦЮ В СИСТЕМІ Si-Mn

Ш.Б. Утамурадова, Ш.Х. Далієв, Дж.Дж. Хамдамов, Х.Дж. Матчонов, А.Х. Хайтбаєв

Інститут фізики напівпровідників та мікроелектроніки Національного університету Узбекистану, вул. Янги Алмазара, 20, Ташкент, Узбекистан

Було проведено комплексне дослідження термічно індукованих фазових перетворень у системі кремній-марганець (Si–Mn). У дослідженні використовувалися рентгенівська дифракція (XRD), раманівська спектроскопія (включаючи хімічне раманівське картування), скануюча електронна мікроскопія з енергодисперсійною рентгенівською спектроскопією (SEM-EDS), глибокорівнева перехідна спектроскопія (DLTS) та термодинамічне моделювання CALPHAD. Послідовність перетворень була надійно реконструйована наступним чином: (i) міжвузлове включення Mn та часткова аморфізація приповерхневого шару Si; (ii) зародження та ріст MnSi (структура B20, $P2_13$); (iii) стабілізація вищої силіцидної фази Mn_4Si_7 в умовах, збагачених Si; (iv) при $T \gg 900$ °C, часткове зворотне перетворення до MnSi. Аналіз DLTS виявив три електрично активні центри глибокого рівня з енергіями активації E_c–0,53 еВ, E_c–0,43 еВ та E_c–0,20 еВ ($\sigma_n \approx 10^{-16}$–$10^{-15}$ см²), які корелюють з переходом MnSi → Mn_4Si_7 та інтерфейсними пастками на межі «силіцид/Si». Моделювання CALPHAD підтвердило негативні вільні енергії Гіббса утворення (ΔG_f) та визначило термодинамічні вікна стабільності для MnSi (600-750°C) та Mn_4Si_7 (800–950°C). Отримана карта процесу забезпечує технологічні параметри для синтезу CMOS-сумісних структур Si–Mn.

Ключові слова: *кремній; марганець; силіциди марганцю; MnSi; Mn_4Si_7; фазові перетворення; рентгенівська дифракція; раманівська спектроскопія; CEM-EDS; DLTS; CALPHAD; вільна енергія Гіббса*